

Near-field acoustical holography and acoustic power analysis of a simulated, highly heated supersonic jet

Kevin M. Leete,^{1,a)}  Kent L. Gee,¹  Junhui Liu,² and Alan T. Wall³

¹Department of Physics and Astronomy, Brigham Young University, Provo, Utah 84602, USA

²Naval Research Laboratory, Washington, DC, 20375, USA

³Battlespace Acoustics Branch, 2610 Seventh Street, Building 441, Wright-Patterson AFB, Ohio 45433, USA

ABSTRACT:

Although near-field acoustical holography (NAH) and acoustic intensity analysis have previously been used to investigate the apparent jet noise sources produced by military aircraft, explicit connections to supersonic jet characteristics cannot be made due to a lack of information about the exhaust plume. To begin to bridge this gap and better understand the source information yielded by NAH, the current study instead applies NAH to a virtual measurement of the near-field pressures of a highly heated laboratory-scale supersonic jet generated by large-eddy simulation (LES). The holographic reconstructions of the pressure, particle velocity, and acoustic intensity are found to match the LES-generated acoustic field well and are used to calculate the acoustic power of the jet. The jet's calculated overall acoustic power is compared to the free-stream mechanical power, resulting in an acoustic efficiency of 1.5%. Ray-tracing of the acoustic intensity to the jet centerline generates an axial distribution of the acoustic power origin, showing that almost all the power originates from the supersonic portion of the flow and with the distribution peak upstream of the potential core tip. Holographic reconstruction of the pressures along the nozzle lipline captures the general spectral shape of the LES-generated pressures, though it underestimates the amplitude.

<https://doi.org/10.1121/10.0009827>

(Received 20 September 2021; revised 7 February 2022; accepted 2 March 2022; published online 23 March 2022)

[Editor: Xun Huang]

Pages: 1989–2001

I. INTRODUCTION

Since the beginnings of jet noise research more than a half-century ago, an ongoing problem has been to understand the spatial distribution of the jet noise source. A variety of methods have played a role in experimentally deriving the locus of acoustic energy in the flow, including measurements using spherical or elliptic reflector directional microphone systems (Laufer *et al.*, 1976; Tam *et al.*, 2008), ray-traced measurements of acoustical intensity (Gee *et al.*, 2017; Jaeger and Allen, 1993; Stout *et al.*, 2015), phased array methods including near-field acoustical holography (NAH) (Leete *et al.*, 2021; Long, 2008; Shah *et al.*, 2015; Wall *et al.*, 2016) and beamforming (Harker *et al.*, 2019; Papamoschou *et al.*, 2019; Podboy *et al.*, 2010), and correlations between the measured flow and acoustic fields (Panda *et al.*, 2005; Papamoschou *et al.*, 2010).

Of particular relevance to the current work is the recent measurement and analysis of the noise fields of highly heated supersonic jets generated by high-performance military aircraft. Phased array methods, such as beamforming (Harker *et al.*, 2019) and near-field acoustical holography (Leete *et al.*, 2021; Wall *et al.*, 2016), have been successful in reconstructing the jet noise field over a large area and have provided estimates of the acoustically relevant source region as a function of frequency. The source estimations

involved either reconstructions of the cross-spectral matrix of a distribution of sources along the jet centerline in the beamforming case, or reconstructions of the pressure field along the nozzle lipline in the holography case. Because measurements of flow variables of these military aircraft are unavailable, whether these source strength or pressure reconstructions are representative of actual measurements of acoustic variables or if they highlight the origin of acoustic power in the plume is left unknown.

Advancements in numerical simulations of jets have allowed for increasingly accurate reproductions of the flow field and acoustic radiation (Bodony and Lele, 2008; Bres and Lele, 2019) and now provide unique opportunities to investigate high temperature, supersonic flows. Many recent works have used decompositions of flow data generated by large-eddy simulations (LES) to gain insight into jet noise source characteristics (such as Faranosov *et al.*, 2017; Jordan *et al.*, 2017; Schmidt *et al.*, 2018; Unnikrishnan *et al.*, 2018 to name a few) as well as the application of inverse methods that are generally reserved for laboratory and full-scale measurements to simulated datasets (Du and Morris, 2012; Leete *et al.*, 2020).

Parallel to investigations of the noise source of jets at the laboratory and full-scales, a great deal of work has been done to predict the noise generated by rockets during launch, generally focusing on semi-empirical representations of the acoustic power of the plume. NASA SP-8072

^{a)}Electronic mail: KevinMatthewLeete@gmail.com

(Eldred, 1971; Lubert *et al.*, 2022) provides normalized spectra, estimates of axial distributions of overall acoustic power, and sound source position as a function of frequency that were generated using laboratory-scale supersonic jet and full-scale rocket data (Horvay and Nagamatsu, 1970; Potter, 1968). The document presents a method to apply these generalized spectra by scaling to the specific test at hand to create an equivalent source model of the jet noise, consisting of a distribution of sources along the jet centerline. The strength of these sources is related to the mechanical power of jet through an assumed acoustic efficiency of about 0.5%. A recent investigation (Gee, 2021) has shown that a plotting error propagated in the NASA SP-8072 document has led to an understanding in the rocket noise community that the main source of noise is the subsonic portion of the flow (Sutherland, 1993), while in the jet noise community, it is understood that the main acoustic power originates between the potential and supersonic cores (Horvay and Nagamatsu, 1970).

The purpose of this paper is to use methods generally applied to full-scale measurements of highly heated supersonic jets and rockets to investigate an LES of a highly heated laboratory-scale supersonic jet. The sound power of the jet is calculated from the simulated pressure and particle velocity fields directly and compared with holography-derived fields. The work both validates previous characterizations of military aircraft sources using NAH and provides new insights into heated, supersonic jet noise sources and radiation. Section II discusses the LES database used in this study. Section III defines acoustic and mechanical energy quantities used. Section IV discusses the holography methodology. Section V compares the holographic reconstructions to the LES-generated field. Section VI discusses the axial distribution of acoustic power as a function of frequency.

II. LARGE-EDDY SIMULATIONS

The LES dataset used in this work is provided by Liu *et al.* (Liu *et al.*, 2015; Liu *et al.*, 2016; Liu *et al.*, 2017), whose prior publications contain more details about the simulation, and plots of the flow acoustic near and far-field distributions. To summarize, they used the Jet Engine Noise Reduction (JENRE[®]) solver to calculate the heated flow passing through a convergent/divergent nozzle. The JENRE[®] solver uses a monotonically integrated LES approach with a flux-corrected transport algorithm (Löhner *et al.*, 1987) and explicit Taylor–Galerkin scheme. Tetrahedral meshes were used to implement the nozzle geometry, which had a nozzle exit diameter, D , of 7.28 cm, a fully expanded Mach number of 1.5, a design nozzle pressure ratio of 3.7, and fully expanded jet velocity, U_j , of 1175 m/s. The thermodynamic quantities in the flow region were calculated out to a conical surface outside of the main flow, then the far-field pressures were predicted using the Ffowcs Williams and Hawkings (FW-H) integration method (Lyrintzis, 2003). Near the nozzle, cell sizes are about $D/286$ and gradually increase to

around $D/20$ near the FW-H integration surface (FWHS). Specifics of the choice of integration surface and grid resolutions can be found in Liu *et al.* (2012).

The simulation was run at a nozzle pressure ratio of 4.0 and a total temperature ratio of 7.0, with an ambient pressure of 98.6 kPa and ambient temperature of 300 K. These parameters resulted in an underexpanded, shock-containing jet with a temperature in a similar regime as high-performance military aircraft operating at afterburner (Walton and Burcham, 1986). A method for calculating the temperature-dependent specific heat ratio was incorporated, which was found to match well with NIST databases for air under these conditions (see Fig. 2 of Liu *et al.*, 2016). Time records of the LES simulation were split into 97 blocks with 50% overlap and a Fourier transform applied to each block to give a complex pressure spectrum with a frequency resolution of about 150 Hz. The total temporal duration of the simulation was 0.326 s, which covers 5260 convective time units (D/U_j). The long simulation was necessary to generate enough blocks for accurate estimation of cross-spectra.

The fluctuating component of pressure and particle velocity generated by the LES are sampled along three simulated arrays: along the jet centerline and the nozzle lipline, sampled from the nozzle exit to $x/D = 25$ in increments of $x/D = 0.2$, and along the FWHS on the line $y/D = \frac{1}{6}x/D + 1.5$ sampled from $x/D = 0$ to $x/D = 25$ in x/D increments of 0.1. The acoustic pressures generated from the FW-H integration are then sampled along three simulated arrays in the field. The first, which is the hologram, is parallel to the FWHS and is described by the equation $y/D = \frac{1}{6}x/D + 10$, with x/D sampled in increments of 0.1 from $x/D = -10$ to $x/D = 40$. This array is expanded by rotating it around the x axis in 20° increments to make a set of 18 finely sampled lines. Another is a single line above the x axis extending from $x/D = -40$ to $x/D = 65$ at $y=0$ and $z/D = 40$ in steps of 0.1 diameters. The last is a far-field arc with radius of $100D$, spanning jet inlet angles (θ) of 45° – 165° in 1° increments, which is rotated about the x -axis in 22.5° increments to make a surface covering the angular range of interest. Figure 1 contains a two-dimensional plot of the location of the nozzle, the sampled arrays along the lipline, FWHS,

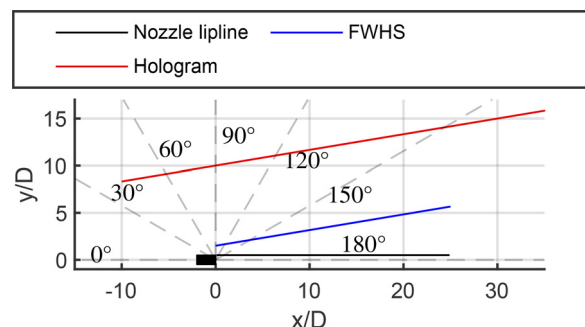


FIG. 1. (Color online) Sampled arrays in the near field: Jet lipline, FWHS, and hologram. Dashed lines show the jet inlet angle, θ .

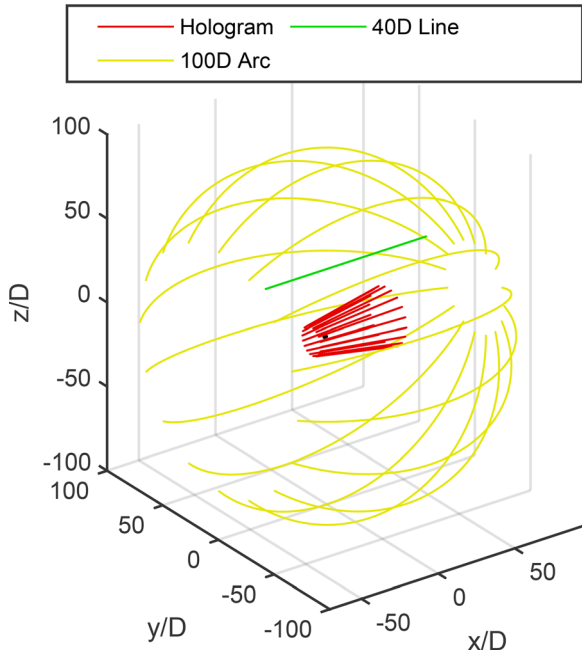


FIG. 2. (Color online) Additional sampled arrays, hologram, 40D line, and 100D arc.

and hologram, while Fig. 2 shows a three-dimensional plot of the expanded hologram, the 40D Line, and 100D Arc.

The local Mach number of the fluid (solid) and the ratio of the axial fluid velocity, U_x , to the fully expanded jet velocity, U_j (dashed) along the jet centerline is plotted in Fig. 3. The end of the potential core (L_c) is estimated as $x/D = 7.2$, where $U_x/U_j \approx 0.95$ and is marked with a square. The end of the supersonic core (L_s), where $M = 1$, is located at $x/D = 12.7$ and is marked with a diamond.

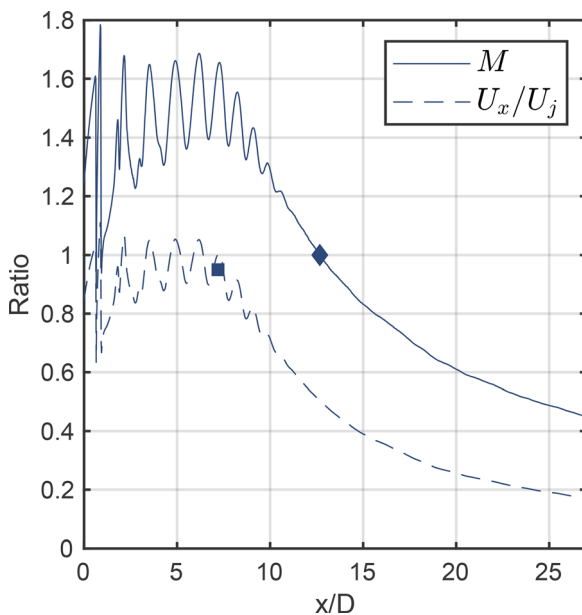


FIG. 3. (Color online) Two dimensionless parameters, the Mach number (solid) and jet velocity ratio (dashed) along the jet centerline, with the locations of L_c (square) and L_s (diamond).

The frequency-dependent complex pressure (p) and particle velocities (u) shown in this work are the outputs of the discrete Fourier transform, scaled to give the correct single-sided power spectrum (in Pa^2) when the modulus squared is averaged over measurement blocks. Sound pressure levels (SPL) are referenced to $20 \mu\text{Pa}$. The sound velocity level (SVL) is calculated as the magnitude of the particle velocity vector referenced to 50 nm/s .

A snapshot of the pressure and velocity fluctuations of the jet are displayed in Fig. 4. The ratio of the pressure to the ambient pressure (P/P_0) is displayed in grayscale, with the magnitude of the velocity vector ($|\vec{U}|$) in color superimposed on top. The color scale shows the range of velocities, though those below the ambient sound speed, c_0 , are cut off. Directional acoustic radiation is seen at a jet inlet angle of 115° , which slowly increases towards the aft to settle at an inlet angle of almost 140° (Liu *et al.*, 2016). The 115° radiation angle agrees well with a predicted value of 112° based on Tam’s vortex sheet model for Mach wave radiation (Tam, 2009). Additionally, the frequency content radiating at this angle was found to correlate with pressure fluctuations along the nozzle lipline originating from the supersonic portion of the jet, upstream of $x/D = 12.7$ (Leete *et al.*, 2020). The far aft radiation with the larger directivity was found to contain correlate primarily with nozzle lipline pressures in an extended region centered around the end of the supersonic core, and has been described as large-scale turbulent structure noise (Leete *et al.*, 2020; Liu *et al.*, 2016).

III. ACOUSTIC AND MECHANICAL ENERGY QUANTITIES

A. Acoustic power

The instantaneous acoustic intensity is the product of the pressure and particle velocity fluctuations at a given point in space (denoted by the position vector \vec{r}). The time-averaged intensity (also called the active intensity) describes the net flow of energy carried by the propagating acoustic wave and can be calculated in the frequency domain (Fahy, 1989) by

$$\vec{I}(f, \vec{r}) = \text{Re}\{G_{p\vec{u}}(f, \vec{r})\}, \tag{1}$$

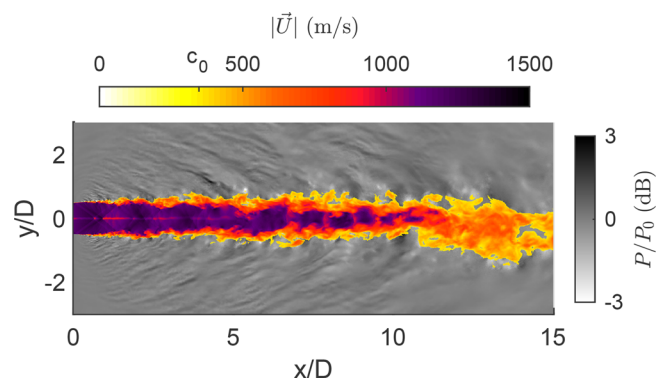


FIG. 4. (Color online) Snapshot of the instantaneous pressure ratio P/P_0 in grayscale, with magnitude of the velocity $|\vec{U}|$ superimposed. Velocities below the ambient sound speed (c_0) are cut off.

where $G_{p\vec{u}}(f, \vec{r})$ is the single-sided cross-spectrum between the pressure and particle velocity. The sound intensity level (SIL) is referenced to 1 pW/m^2 , so that it is the same as the SPL and SVL in the case of plane and spherical wave propagation.

The total acoustic power (W_a) of a source can be calculated by defining a closed surface, S , surrounding it and integrating the intensity flowing out of that surface,

$$W_a(f) = \int_S \vec{I}(f, \vec{r}) \cdot \vec{n} dA, \quad (2)$$

where \vec{n} is the unit normal vector of the surface pointed outward and dA is the differential area on the surface.

This computation is made simple when the integration surface is situated in the far field, such that the acoustic field can be approximated as locally planar. If a measurement surface is then chosen that is parallel to the planar wavefronts, the dot product in Eq. (2) reduces to multiplication of the intensity magnitude with the corresponding area of the surface. Additionally, for plane wave propagation, the intensity vector magnitude can be approximated simply by the scaled autospectrum of the pressure, $G_{pp}(f, \vec{r})$, as

$$|\vec{I}(f, \vec{r})| \approx \frac{G_{pp}(f, \vec{r})}{\rho_0 c}. \quad (3)$$

The single-sided autospectra of the pressures are estimated by averaging the magnitude squared of the Fourier transform of the pressure waveform over all the 97 simulated blocks, and likewise, the autospectra of each component of the particle velocity. The cross-spectra between the pressure and each particle velocity component are estimated by the average over blocks of the Fourier transform of the pressure times the conjugate of the Fourier transform of the particle velocity.

B. Mechanical power and acoustic efficiency

The acoustic efficiency (η) of a jet is the ratio of radiated acoustic power, W_a , to the total mechanical power of the jet, W_m ,

$$\eta = W_a/W_m. \quad (4)$$

For a jet with position-dependant flow velocity vector, $\vec{U}(\vec{r})$, and density, $\rho(\vec{r})$, the mechanical power is determined by the flux of the kinetic energy density, $k(\vec{r}) = \frac{1}{2}\rho(\vec{r})|\vec{U}(\vec{r})|^2$, through the nozzle exit area (A_e):

$$W_m = \int_{A_e} k(\vec{r})(\vec{U}(\vec{r}) \cdot \vec{n}) dA. \quad (5)$$

If k and \vec{U} are axisymmetric and \vec{U} is perpendicular to the nozzle exit plane, Eq. (5) reduces to

$$W_m = \pi \int_0^{D/2} \rho(r)|\vec{U}(r)|^2 U_x(r)r dr, \quad (6)$$

where r is the radial distance from the jet centerline.

Numerical integration over the nozzle exit is straightforward using the parameters calculated from the LES. For the current simulation, the integration completed at the $x/D = -0.1$ plane (to avoid expansion and recirculation effects at the nozzle exit) results in $W_m = 769.0 \text{ kW}$.

In investigations of rocket noise at launch, the expression in Eq. (6) is often simplified by assuming that $|\vec{U}| = U_x$ and that ρ and $|\vec{U}|$ are constant over the nozzle exit plane, resulting in

$$W_m = \frac{1}{8}\pi D^2 \rho U_x^3. \quad (7)$$

Use of the centerline velocity and density at the nozzle exit in Eq. (7) significantly underestimates W_m , due to the presence of a Mach disk close to the nozzle exit. To avoid these, as well as other effects of the geometry of the nozzle, the fully expanded nozzle diameter, velocity, and density can be used instead (Varnier, 2001). This substitution results in $W_m = 847.5 \text{ kW}$, an overestimation error of 10.2% for this simulation.

IV. HOLOGRAPHY METHOD

The holography method used in this work is called statistically optimized near-field acoustical holography (SONAH), which was developed by Steiner and Hald (2001) to overcome the requirement of traditional Fourier-based Holography that the measurement aperture must be much larger than the source. Section IV A discusses the basic formulation of the technique to estimate the pressures of a coherent field. Section IV B discusses how the formulation is altered to estimate the particle velocity fluctuations. Section IV C discusses application to the partially-coherent jet noise field of the LES.

A. SONAH formulation

Statistically optimized near-field acoustical holography can be thought of as a two-step process: First, an equivalent wave model (EWM) is fit to a hologram surface, h , and second, that EWM is evaluated at a reconstruction surface, q . The EWM used in this study is a set of m cylindrical basis functions, $\Psi(\vec{r})$, where

$$\Psi_{l,k_x}(\vec{r}) \equiv \frac{H_l^1(k_r r)}{H_l^1(k_r r_0)} e^{il\phi} e^{ik_x x}, \quad r \geq r_0 \quad (8)$$

and r , ϕ , and x are the radial, azimuthal, and axial spatial components of \vec{r} . H_l^1 is the l th-order Hankel function of the first kind; i is the imaginary unit, r_0 is some small reference radius [traditionally the assumed source radius (Cho et al., 2005)], and k_x and k_r are the axial and radial wavenumbers, respectively. For the current work, only $l=0$ wavefunctions were used for consistency with previous work on military aircraft (Leete et al., 2021; Wall et al., 2016). Initial investigations in using additional azimuthal modes in the holography reconstructions have resulted in reduced accuracy in

reconstructed field sound pressure levels and have been left for future work.

Given the choice to only include $l=0$ in Eq. (8), the number of wavefunctions, m , is only dependent on the number of k_x values used. The k_x values for this study were regularly spaced between $-\pi/dx$ and π/dx , in steps of $2\pi/(8\Delta x)$ with dx as the interelement spacing of the virtual array in x and Δx is the total span of the virtual array in x . This simulates an aperture eight times larger than what was input, which was found to be necessary to eliminate wraparound errors over the region investigated in this work. The radial wavenumbers are

$$k_r = \begin{cases} \sqrt{k^2 - k_x^2} & \text{for } |k| \geq |k_x|, \\ i\sqrt{k_x^2 - k^2} & \text{for } |k| < |k_x|, \end{cases} \quad (9)$$

where $k = \omega/c$ is the acoustic wavenumber, ω is the angular frequency, and c is the speed of sound. This choice for wave function and definition of k implies a time harmonicity of $e^{-i\omega t}$.

For a hologram measurement of n_h sample points, the EWM evaluated at that location is constructed into a matrix \mathbf{A} where the ij th element of \mathbf{A} is the i th wavefunction evaluated at the j th point

$$\mathbf{A}_{ij} = \Psi_{k_{xi}}(\vec{r}_j), \quad (10)$$

where the size of \mathbf{A} is m by n_h . A similar matrix, α , is generated in the same way, but with the EWM evaluated at the reconstruction surface. This matrix has the same number of rows as \mathbf{A} , but with columns equal to the number of points at which to reconstruct, n_q .

At this point, the SONAH process (Steiner and Hald, 2001) calculates the column vector of pressures at q , \mathbf{p}_q , from the column vector of pressures on h , \mathbf{p}_h ,

$$\mathbf{p}_q^T = \mathbf{p}_h^T \mathbf{R}_{\mathbf{A}^H \mathbf{A}} \mathbf{A}^H \alpha, \quad (11)$$

where the superscript T is the transpose, H is the Hermitian transpose, and $\mathbf{R}_{\mathbf{A}^H \mathbf{A}}$ is the regularized inverse of $\mathbf{A}^H \mathbf{A}$. Regularization is performed using a modified Tikhonov filter with the generalized cross-validation procedure for the selection of the regularization parameter as outlined in Williams (2001).

Since the matrix α is simply the set of chosen wavefunctions evaluated at q , all the preceding multiplications in Eq. (11) can be combined to represent the transpose of the column vector of coefficients corresponding to those wavefunctions, \mathbf{c}^T . Thus, Eq. (11) can be simplified to

$$\mathbf{p}_q^T = \mathbf{c}^T \alpha. \quad (12)$$

B. Particle velocity

It is a straightforward procedure to use the EWM to reconstruct the three components of particle velocity in addition to the pressures at the desired location. Following the process outlined in Stout *et al.* (2018), the particle

velocity of acoustic waves in a source-free medium is related to the pressure *via* Euler's equation for a linearized, time-harmonic acoustic process,

$$\vec{u}(\vec{r}) = -\frac{i}{\omega \rho_0} \nabla p(\vec{r}), \quad (13)$$

where ω and ρ_0 are the angular frequency of interest and the ambient density of the medium, respectively. The column vector of the radial, azimuthal, and axial components of the particle velocity evaluated at the reconstruction location can be calculated by simply applying Eq. (13) to Eq. (12). For clarity, these three components of the particle velocity are separated into Eqs. (14)–(16),

$$\mathbf{u}_{rq}^T = \mathbf{c}^T \left(\frac{-i}{\omega \rho_0} \right) \nabla_r \alpha, \quad (14)$$

$$\mathbf{u}_{\phi q}^T = \mathbf{c}^T \left(\frac{-i}{\omega \rho_0} \right) \nabla_\phi \alpha, \quad (15)$$

$$\mathbf{u}_{zq}^T = \mathbf{c}^T \left(\frac{-i}{\omega \rho_0} \right) \nabla_z \alpha, \quad (16)$$

where the subscripts on the gradient operator represent the component of the gradient in that particular direction, and the gradient operation is element-wise. The entries of α are the wavefunctions described in Eq. (8), whose three components of the gradient in cylindrical coordinates are well known:

$$\nabla_r \Psi_{l,k_x}(\vec{r}) = \frac{l H_l^1(k_r r) - k_r H_{l+1}^1(k_r r)}{H_l^1(k_r r_0)} e^{il\phi} e^{ik_x x}, \quad (17)$$

$$\nabla_\phi \Psi_{l,k_x}(\vec{r}) = \frac{il}{r} \Psi_{l,k_x}(\vec{r}), \quad (18)$$

and

$$\nabla_x \Psi_{l,k_x}(\vec{r}) = ik_x \Psi_{l,k_x}(\vec{r}). \quad (19)$$

Thus, once \mathbf{c}^T is obtained, both the pressure and particle velocity components can be computed for an arbitrary choice of reconstruction location. However, because of the axisymmetric assumption ($l=0$) made in this work, the ϕ component of the gradient in Eq. (18), and the subsequent $\mathbf{u}_{\phi q}$ in Eq. (15), are identically zero for any choice of q .

C. Application to LES

A fundamental assumption of SONAH is that the field at each frequency is a solution to the homogeneous Helmholtz equation, meaning that the field is coherent and contains no acoustic sources in the region between the hologram and the reconstruction location. It is well known that the jet noise field is not self-coherent, so care must be taken to extract self-coherent partial fields, apply the holography process to each partial field individually, then sum the partial fields together at the reconstruction location to arrive at

a final answer (Hald, 1989). First, a data matrix is constructed where the ij th element is the complex pressure measured for the j th block at the i th measurement point along the array; then, this matrix is multiplied by its Hermitian transpose to generate the cross-spectral matrix (CSM) of the array. The singular value decomposition of the CSM is then used to obtain the partial fields, which are simply each singular vector scaled by the square root of its corresponding singular value. This method for extracting partial fields (or modes) that are coherent in space and time is more recently known as the spectral proper orthogonal decomposition (Schmidt and Colonius, 2020).

For the current study, each simulated array in use contains many more elements than there are measurement blocks, so the rank of the CSM (and therefore, the number of meaningful partial fields) is limited to the number of blocks, which is 97. Each of the 97 partial fields has a unique shape, though a common trend of these decompositions is that the partial field shapes are reminiscent of modes on a string, where the first has a single antinode at the point of maximum SPL, the second has two antinodes to the sides of the maximum, the third has three straddling the two from the second field, and so on. This causes the higher-order partial fields to have large amplitudes at the edges of the array relative to their peak.

To minimize wavenumber leakage caused by abrupt changes at the edges of the array, each partial field is extended two acoustic wavelengths in both directions using analytic continuation (Williams, 2003), then windowed with a Tukey window to enforce a graceful taper to zero. For this paper, the vectors \mathbf{p}_h and \mathbf{p}_q used in Eq. (11) are populated by the complex pressures at a particular partial field after this extension has been applied.

The bulk of the computation time at each frequency is spent in the regularization and inversion of the matrix $\mathbf{A}^H\mathbf{A}$, whose size is n_h by n_h . To reduce the size, the hologram can be resampled so that the interelement spacing is larger, as long as spatial aliasing is avoided at that frequency. For this analysis, the array was decimated to an interelement spacing so that there were three points per wavelength, with a minimum of 97 elements to preserve the rank of the CSM.

V. RESULTS

This section discusses the similarity of the holographic reconstruction of the pressure, particle velocity, and acoustic intensity to the LES-generated data. Field reconstructions are compared along the 100D Arc and the FWHS to check ability of the reconstructions to recreate the acoustic field as a baseline, then the reconstructions are extended inward toward the nozzle lipline to investigate possible similarities to the LES-generated data.

A. Far-field reconstructions

Sound pressure level and reconstruction accuracy in the far field are displayed in Fig. 5, which in part (a) shows the spectra along one of the simulated arc arrays (yellow lines

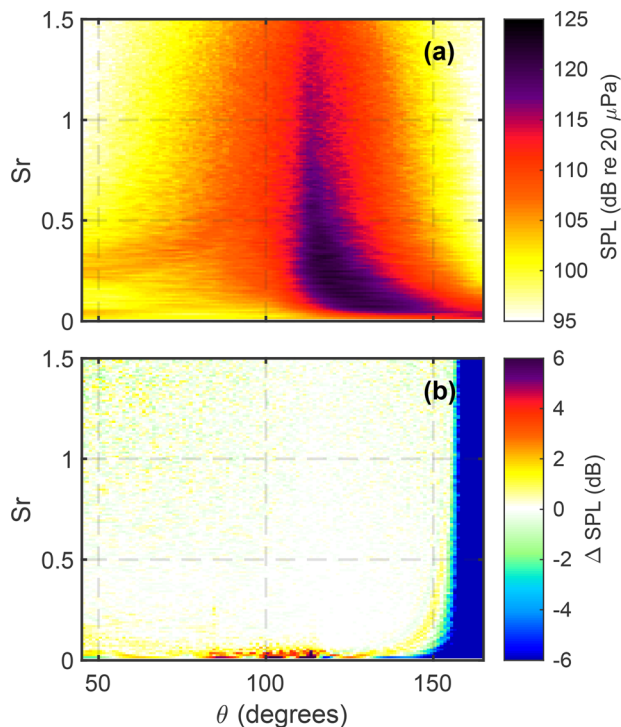


FIG. 5. (Color online) (a) Pressures along the far-field arc, (b) error in the reconstruction as a function of jet inlet angle (θ) and Strouhal number.

in Fig. 2) as a function of jet inlet angle, θ , the color representing the narrowband SPL. The frequencies are expressed in terms of Strouhal number, $Sr = fD/U_j$. The level is nearly axisymmetric along these far-field arcs, with variations of consistently less than 1 dB from arc to arc.

The change in spectra as a function of inlet angle follows the expectation for supersonic laboratory-scale jet noise; the noise peak frequency is high towards the sideline and steadily decreases aft, with a peak Strouhal number of about 0.2 in the maximum radiation direction. Broadband shock-associated noise is also seen radiating in the forward direction, with the characteristic leftward-curving shape at $Sr < 0.5$ for $\theta < 90^\circ$ (Nielsen *et al.*, 2019). Figure 5(b) shows the LES-generated level from part (a) subtracted from the NAH-reconstructed level. Negative values represent underestimation of the NAH reconstructions and positive values represent overestimation of the NAH reconstructions.

Less than 1 dB error for the majority of the spatio-spectral domain is observed, except at $Sr < 0.06$ and angles greater than 155° . Underestimation in the far aft radiation is due to the tapering of the pressures outside of the hologram to zero as discussed in Sec. IV C.

B. FWHS reconstructions

Reconstructions along the FWHS indicate to what degree the EWM is successful at representing all the acoustic and hydrodynamic information, as the pressures at the hologram (the input to the NAH process) originally came from FWH-integration from that surface. Figure 6 shows the

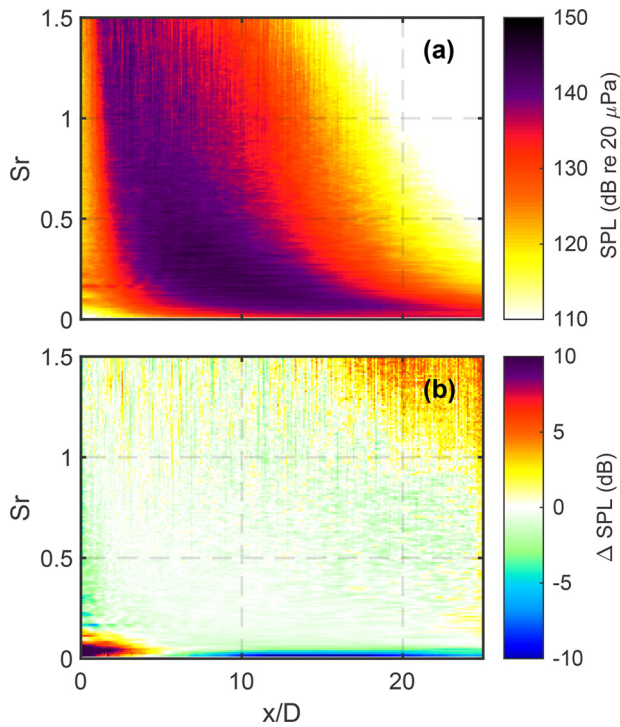


FIG. 6. (Color online) (a) Pressures along the FWHS, (b) error in the reconstruction as a function of distance from the nozzle in diameters and Strouhal number.

pressures generated by the LES in part (a) and reconstruction errors in part (b) in the same format as Fig. 5. The reconstructions are accurate to within 2 dB error in most of the frequency and spatial range shown, though with large errors at the lowest frequencies and near the nozzle exit. Additionally, overestimations of the field by about 6 dB are found at $Sr > 1$ at the far downstream locations.

The LES-generated data contain particle velocities as well as pressures along the FWHS, so the magnitude of the particle velocity vector, $|\vec{u}|$, reconstructed at the FWHS array is compared to the simulation in Fig. 7 and is displayed as a SVL. Errors are similar to those of Fig. 6, though with slightly larger amplitudes and the addition of large underestimations of the field far downstream. These underestimations in the far aft region are due to the windowing of the hologram explained in Sec. IV C and indicate that the chosen hologram was not large enough to fully reconstruct the field over the entire FWHS.

The SIL calculated along the FWHS array is displayed in Fig. 8. The similarity in the spectral shape of the SIL and the SPL indicate that much of the field energy is contained in the acoustically propagating components. Generally, the SPL, SVL, and SIL are overestimated by NAH in areas where amplitudes are low: by the nozzle exit at low frequency and far aft at high frequency. Low-frequency levels are underestimated downstream of the nozzle, and the SVL is underestimated at the far aft edge of the array at all frequencies. Since the pressures along the FWHS are the output from the LES, it is unclear if the error in the reconstruction at low frequencies is due to the hologram not containing

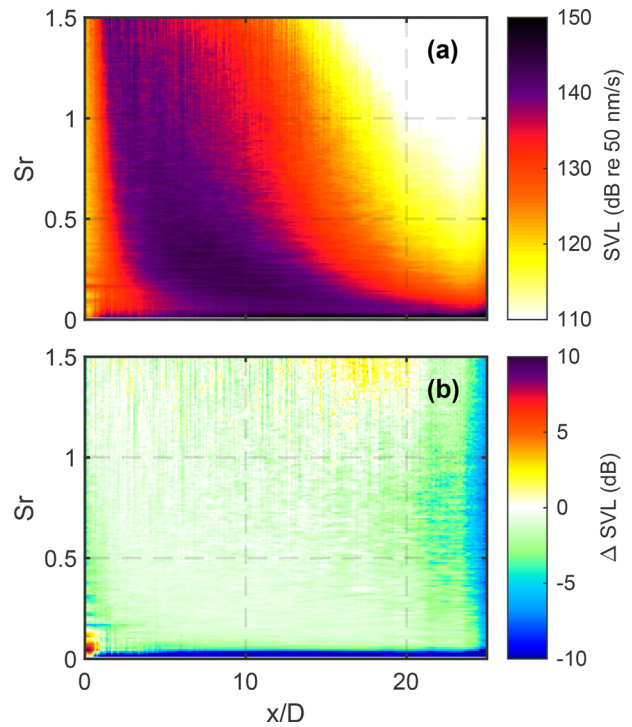


FIG. 7. (Color online) (a) SVL along the FWHS, (b) error in the reconstruction as a function of distance from the nozzle in diameters and Strouhal number.

enough non-radiating pressure components (for example, if the FW-H integration from the FWHS to the hologram did not transfer the hydrodynamic components) or if simply the hologram was chosen too far away from the jet flow, such

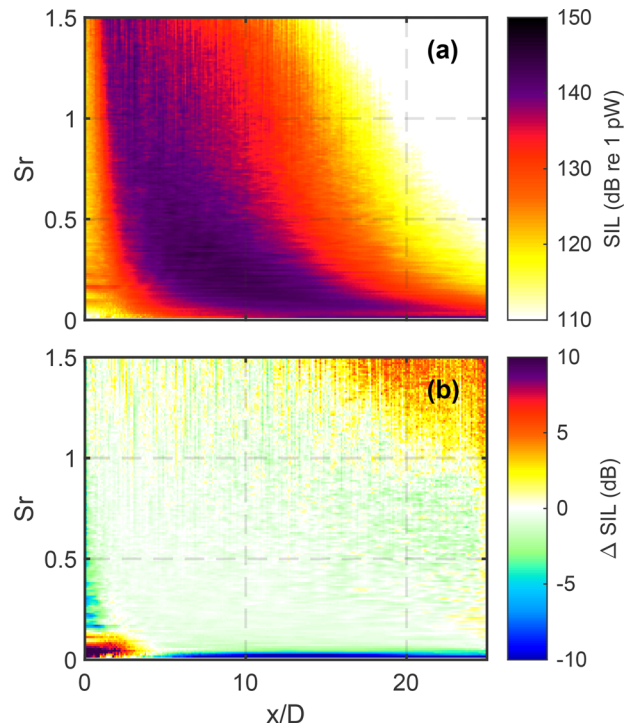


FIG. 8. (Color online) (a) Intensity magnitude along the FWHS, (b) error in the reconstruction as a function of distance from the nozzle in diameters and Strouhal number.

that the evanescent components of the pressure field had already decayed.

C. Lipline reconstructions

Previous works using NAH on military aircraft noise fields (Leete *et al.*, 2021; Wall *et al.*, 2016) have used reconstructions of the pressure field along the nozzle lipline to illuminate trends in the source of acoustic power in the jet plume. Though holographic reconstruction of the field is not expected to reproduce the actual field along the nozzle lipline, it is of interest to investigate the similarities between the reconstructed and true fields to better understand the significance of the NAH-derived “apparent” or “equivalent” sources. Figure 9 shows this comparison, with part (a) displaying the LES-generated pressures sampled along the nozzle lipline, part (b) the NAH pressure reconstructions, and the difference in part (c).

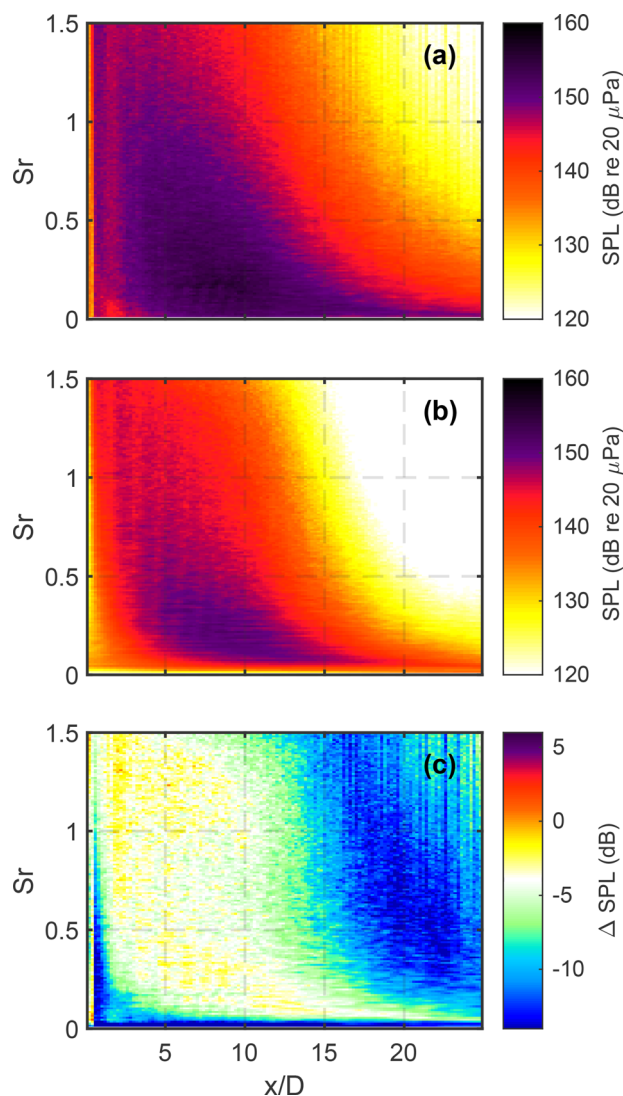


FIG. 9. (Color online) (a) LES pressures, (b) reconstructed pressures, (c) error in the reconstruction along the nozzle lipline as a function of distance from the nozzle in diameters and Strouhal number. The color bar is centered at an offset of -4 dB.

In general, errors are due to misrepresentations of the shape of the spectra as well as miscalculation of the overall level. To separate these two types of errors, the color map of Fig. 9(c) is chosen such that white, instead of representing zero, now represents an offset value of -4 dB, calculated as the mean difference of the NAH from the LES reconstructions in the region 3 dB down from the peak in the spatio-spectral domain. With the colormap in part (c) centered around -4 dB, it is seen that after accounting for the underestimation of pressure, the reconstructions otherwise generally follow the relative shape of the spectra well. After adjustment for this offset, errors in the mainlobe are within about 2 dB. However, large errors occur outside of this main locus of energy (downstream of L_s and near the nozzle exit) which are truncated by the range of the color bar so details in the main radiation region can be seen.

The EWM used in the holography method represents waves emanating from a small cylindrical surface which contains all the pertinent sources; the only situation in which the pressures along the nozzle lipline would match the reconstructions is if all the acoustic sources were located within a similar cylinder whose surface is on the lipline. Thinking in terms of Lighthill’s acoustic analogy, the acoustic sources for the jet noise would be distributed throughout the plume, both outside and inside the nozzle lipline. Additionally, the pressure fluctuations generated by the LES (which includes both hydrodynamic and acoustic components) are not necessarily correlated with the sound radiated to the far-field hologram, from which the EWM is derived. An ongoing research problem is to identify flow pressure components that do correspond to the far-field acoustics, such as the application of Doak’s momentum potential theory (Unnikrishnan *et al.*, 2018) or other flow-field decompositions (Taira *et al.*, 2017).

The fact that the shape of the reconstructed pressure spectra along the lipline matches that of the LES-generated data suggests the acoustic component of the pressures is significant along the nozzle lipline (Adam *et al.*, 2021; Leete *et al.*, 2020). This is likely because of the supersonic nature of this jet, which allows for the pressure fluctuations to propagate to the field via the Mach wave radiation mechanism. Additionally, of note is the fact that no refraction effects in the plume are incorporated in the EWM, but the reconstructed and lipline pressure spectral shapes still line up spatially.

The similarity between the pressure reconstructions in the supersonic portion of the flow suggest that this source region is efficient, with the pressure fluctuations of the flow matching the acoustic field fluctuations. Conversely, the fluctuating pressures in the subsonic portion of the flow are severely underestimated by NAH, suggesting that the acoustic field is only a small portion of the fluctuating energy there (with the exception of some low-frequency components near $Sr = 0.1$).

VI. ACOUSTIC POWER ANALYSIS

For better understanding of the acoustic properties of the jet, the overall acoustic power is calculated where LES-

generated pressure and particle velocities are available to calculate the vector intensity. This calculation is compared to calculations done outside the FWHS using the pressures and particle velocity fields reconstructed by NAH, and repeated with results from the pressure reconstructions alone using the assumptions of Eq. (3). Axial distributions of the origin of the overall acoustic power are then derived by ray-tracing the intersection of the acoustic intensity vectors in the field with the jet centerline.

A. Acoustic power

Calculations of W_a of any jet can be achieved with direct application of Eq. (2) if the dataset in question has both pressure and particle velocity sampled with sufficient density on a surface surrounding the jet. In practice, measurement of the particle velocity or vector intensity in field tests are often forgone, resulting in application of the approximations contained in Eq. (3). For each of the sampled arrays mentioned in Sec. II, the calculation of W_a is completed using the LES data directly where both pressure and particle velocities are available and from the holographic reconstructions where they are not. The process is then repeated using Eq. (3) to estimate the intensity magnitude and assuming the acoustic intensity vector is perpendicular to the sampled surface. Table I shows the W_a calculated in each of these situations, with the left column denoting the array used to calculate the acoustic power and the four remaining columns whether the LES data or holographic reconstructions were used along with the method of calculating the vector intensity.

For the extended hologram and 100D Arcs where there is azimuthal information, the calculation was done twice, once using a single array which is rotated around the x axis, and once with the full array. The addition of more azimuthal coverage changed the calculation of W_a by less than 0.01 dB, confirming the axisymmetry of the levels of the jet noise in this simulation. All reported results hereafter are thus completed using a single array with an axisymmetric assumption. The overall acoustic power level is calculated over the frequency band $Sr < 1.5$.

The true value of W_a for this simulation is taken as 160.6 dB, which was calculated on the FWHS using the LES-generated pressure and particle velocity. By design, the FWHS is chosen to capture all the pertinent acoustic energy

TABLE I. Overall acoustic power level (dB re 1 pW) calculated from various arrays.

	LES		Holography	
	Re{ G_{pu} }	$G_{pp}/(\rho_0 c)$	Re{ G_{pu} }	$G_{pp}/(\rho_0 c)$
FWHS	160.6	161.8	159.2	161.4
Hologram	—	160.5	160.3	161.5
40D line	—	160.4	160.2	161.0
100D arc	—	160.5	160.2	160.5
Lipline	145.9	165.5	160.3	160.9
EWM source	—	—	160.3	161.8

which is transferred to the far field, and thus, application of Eq. (2) on this surface is chosen as the baseline for further analysis. Holographic reconstructions along the FWHS slightly underestimate W_a , and both in the data and the reconstructions the level is overestimated by at least 1 dB when using the pressures alone.

At the three field arrays, the hologram, the 40D line, and the 100D arc, the squared pressures of the LES estimate W_a closely, and match the calculation by the NAH reconstruction of the pressure and particle velocity. When holography pressures are used alone, W_a is overestimated but becomes more accurate in the far field. Along the nozzle lipline, the holographic reconstructions preserve the W_a found in the field, but the LES data overestimate the power when using the pressures alone and underestimate the power when the pressure and particle velocity are used. The severe underestimation using the FWHS is due to effectively excluding all the acoustic sources outside of a cylinder with radius on the nozzle lipline.

The overestimation of W_a when the autospectrum of the pressures is used to estimate the vector intensity magnitude is a combination of two factors: first, using G_{pp} instead of G_{pu} to calculate the acoustic intensity does not filter out the hydrodynamic components that do not propagate to the far field and second, the actual intensity vectors are not perpendicular to the surface represented by the array. At the nozzle lipline, the overestimation is mostly due to not filtering out the hydrodynamic components, while at the FWHS, it is a combination of the two effects.

The overall acoustic power calculated for this simulated jet (corresponding to the level of 160.6dB reported in Table I) is 11.48 kW, which results in an acoustic efficiency (η) calculation of 1.5%. This percentage is larger than reported by NASA SP-8072 (Eldred, 1971), which uses 1% as a conservative upper bound for estimating the generated acoustic power from rockets at launch and much larger than the assumed efficiency of $\eta = 0.5\%$, which has been the standard in rocket noise research for decades (Lubert *et al.*, 2022). Using the simplified mechanical power calculation with the ideally expanded conditions leads to $\eta = 1.35\%$, an underestimation of the true value.

B. Axial distribution of acoustic power

Acoustic power calculations for the entire jet are helpful in describing its overall acoustical efficiency; however, information about the origin of this noise can lend insight into noise generation mechanisms within the plume. Previous analyses of this LES dataset (Leete *et al.*, 2020; Liu *et al.*, 2016) investigated the difference between the Mach wave radiation originating upstream of L_s and the large-scale turbulent structure noise originating from L_c to several diameters beyond L_s .

Equation (2) is interpreted as calculating the power flux through an enclosing surface, which, in practice, is discretized into a finite number of patches, each represented by a measurement point. Therefore, the dot product of the

intensity vector with the normal vector of each patch is the power contribution from that patch. The origin of this small portion of the overall power can be found by ray-tracing the intensity vector at that patch back to the jet centerline. Figure 10 shows a schematic of this process on the FWHS superimposed on a snapshot of the pressure fluctuations calculated by the LES. The arrow labelled \vec{I} represents the calculated intensity vector at a particular sampled location and the arrow labelled \vec{n} represents the normal vector to the measurement surface, with the insert showing a zoomed-in version of the point in question. The dashed line trailing from \vec{I} represents the calculation of the source location for this particular patch's worth of power. The dotted line trailing from \vec{n} represents the ray-tracing if the intensity vector is not actually known and its vector magnitude needs to be estimated using Eq. (3). The two vectors' trailing dashed lines would be identical if the measurement surface was chosen to be parallel to the acoustic wavefronts.

When this ray-tracing is completed for all the patches over the enclosing surface S , it results in a list of origins for all the individual patches with their contributing power values. These bits of acoustic power are divided into $\frac{1}{2}D$ bins along the jet centerline, summed over bin, and normalized to the bin width to create $W_x(x)$, the power per dimensionless length, such that the integration of $W_x(x)$ over x results in W_a . Figure 11 shows the results of this ray-tracing procedure for holographic reconstructions of the vector intensity along the 100D arc, the hologram, the direct computation of the vector intensity along the FWHS from the LES, the computation using the squared pressures along the FWHS to approximate the intensity vectors, and the squared pressures of the holographic reconstructions along the nozzle lipline. The values of $W_x(x)$ in Fig. 11 have units of watts per non-dimensional length.

The axial distribution of acoustic power can also be viewed on a frequency-by-frequency basis as an axial distribution of acoustic power spectral density, $W_{xd}(x, Sr)$. Two of these frequency-dependent ray-traced source distributions are displayed in Fig. 12, which shows the acoustic power spectral density traced back to each $\frac{1}{2}D$ bin along the jet centerline from (a) the LES on the FWHS and (b) the holographic reconstructions to the 100D Arc. The powers are represented as a level referenced to 1 pW. The green dashed and dotted lines on Figs. 11 and 12 represent L_c and L_s , respectively.

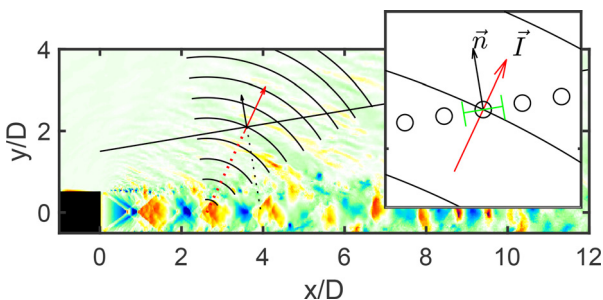


FIG. 10. (Color online) Schematic of ray-tracing procedure overlaid on a snapshot of the instantaneous pressures generated by the LES.

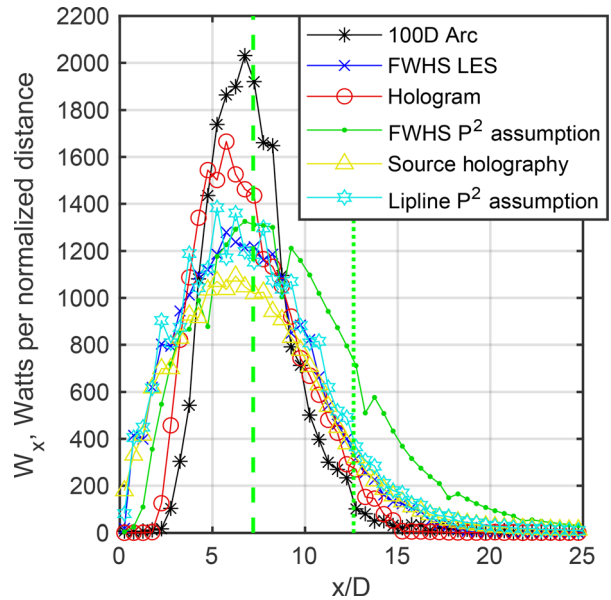


FIG. 11. (Color online) Acoustic power per non-dimensional length along the jet centerline, ray-traced from various field arrays and calculated from SONAH reconstructions on a cylinder of radius r_0 . The vertical dashed and dotted lines represent L_c and L_s , respectively.

Both Figs. 11 and 12 show a trend in the localization of the acoustic power depending on the placement of the array. The calculation of the axial source distribution from the FWHS is broad, though the far-field estimations integrate to the same overall acoustic power level as those derived from the FWHS, they concentrate the energy into a more compact

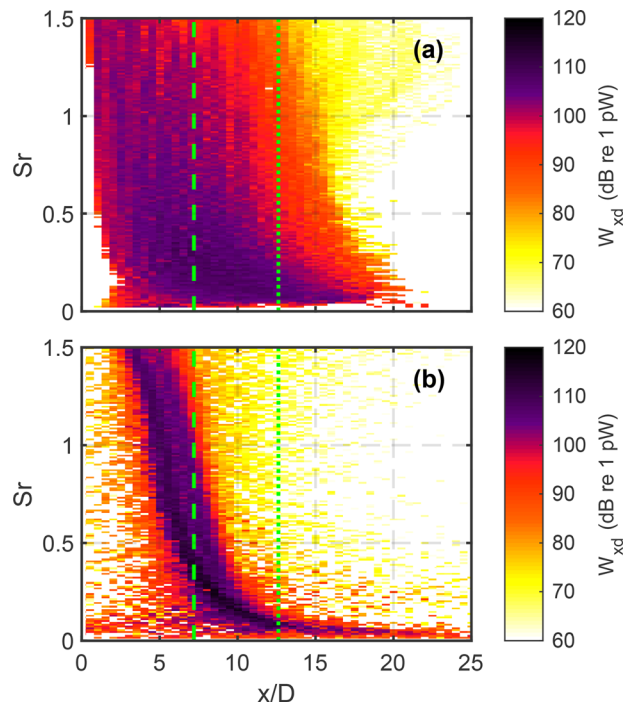


FIG. 12. (Color online) Acoustic power spectral density (W/Sr) level (dB re 1 pW) for the power traced back to $\frac{1}{2}D$ bins along the jet centerline originating from the (a) LES data along the FWHS, (b) the dashed and dotted lines represent L_c and L_s , respectively.

region whose location is highly frequency dependent. The difference between far-field and near-field derivation of the locus of acoustic power highlights the fundamental difference between the acoustic radiation in these two regions, and that even 100D away from the nozzle exit one is not in the true far field, where the spatial origin of the sound should be compact and at the same location at all frequencies.

A way to eliminate the ray-tracing step in the acoustic intensity analysis procedure is to evaluate Eq. (2) directly on the equivalent source of the EWM, a cylinder centered on the x axis with radius of r_0 . This result is captured in the final row of Table I, which underestimates the true W_a by 0.3 dB when using the product of pressure and particle velocity and overestimates when using the G_{pp} assumption by 1.2 dB.

Since the chosen r_0 in this study is small (0.5 mm), the acoustic power per length of the cylindrical radiator approximates the axial distribution of source power along the jet centerline. This is calculated by carrying out the integration of Eq. (2) over the azimuth only, leaving a function of x , $W_x(x)$. When binned appropriately to match the distributions of the ray-tracing procedure, the line labelled “Source holography” in Fig. 11 is the result. Small differences from this result to the ray-tracing of the LES data directly are limited to a portion of energy reallocated from the main peak of the distribution to the downstream tail.

The ground truth calculations of space and frequency dependence of power is taken to be from acoustic intensity calculated directly from the LES along the FWHS [labelled “FWHS LES” in Fig. 11 and part a) of Fig. 12]. In previous NAH studies of the jet noise of high-performance military aircraft (Leete *et al.*, 2021; Wall *et al.*, 2016), pressure reconstructions along the nozzle lipline are given as representative of the jet noise source location, giving the SPL of these pressure reconstructions as an analog for source power. The acoustic power distribution using this method applied to the current simulation is shown in Fig. 11 as the line labelled “Lipline P^2 assumption.”

The shape of the axial distribution of source power along the jet centerline is approximated by the holographic reconstruction of the squared pressures along the nozzle lipline, which is remarkable. As stated previously, the NAH procedure does not contain any information about the flow regions of the jet and does not account for convection effects. Though the NAH reconstructions of the pressure have an amplitude offset from the actual LES-generated pressures, as shown in Fig. 9, this incorrect pressure amplitude represents the correct acoustic power, which NAH maintains consistent wherever it is reconstructed. Since the spatial distribution of the pressures is still representative of the LES, $W_x(x)$ derived from NAH reconstructions along the nozzle lipline does appear to accurately reflect the axial distribution of source power for this simulation. A caveat here is that there is significant wiggle seen in the “Lipline P^2 assumption” line seen in Fig. 11, corresponding to the vertical striations in Fig. 9(b). These striations may be due

TABLE II. Percent of W_a originating from upstream, between, and downstream of the potential (L_c) and supersonic (L_s) cores.

Array	Method	$x < L_c$ (%)	$L_c < x < L_s$ (%)	$L_s < x$ (%)
100D Arc	G_{pu}	52	45	3
Hologram	G_{pu}	54	42	4
FWHS	G_{pu}	53	40	7
FWHS	G_{pp}	37	43	20
Lipline	G_{pp}	51	39	10
Source holography	G_{pu}	51	39	10%

to the effects of the shock cells in the simulation, but require further investigation.

C. Interpretation in terms of L_c and L_s

Differences in source power localization method may change the interpretation of which region of the jet is contributing most to the acoustic power. Gee (2021) has highlighted recently discrepancies on whether the majority of the acoustic power from heated supersonic jets and rockets originates from the supersonic or subsonic regions of the flow. Table II shows the percent of W_a that originates from the potential core ($x < L_c$), between the potential and supersonic cores ($L_c < x < L_s$), and the subsonic portion of the flow ($L_s < x$). Each row of Table II corresponds to the location from which the vector intensity was ray-traced, using the NAH reconstructions. The second column shows whether the vector intensity was calculated using G_{pu} or G_{pp} .

Using G_{pu} at the 100D Arc, the hologram, and the FWHS all result in similar interpretations of the majority of the energy split between upstream of the potential core and between the potential and supersonic cores, even though the corresponding lines in Fig. 11 look different from each other, becoming more compact the further in the field the array is located. This stark difference is illustrated most acutely in Fig. 12 between parts (a) and (b). If, however, G_{pp} is used instead, the intensity vectors are estimated as perpendicular to the integration surface. When this is done at the FWHS, the energy distribution is shifted downstream, resulting in 20% of the energy being localized to the subsonic portion of the flow.

NAH reconstructions of G_{pp} along the nozzle lipline [as have been done in past studies of military aircraft (Leete *et al.*, 2021; Wall *et al.*, 2016)] estimate the source power distribution well, with nearly the same result as using G_{pu} at several arrays where NAH is known to accurately represent the propagating acoustic field. Evaluation of the equivalent cylindrical source of the EWM provides a consistent physical interpretation as well.

VII. CONCLUSIONS AND RECOMMENDATIONS

Statistically optimized near-field acoustical holography is successful in reconstructing the noise produced by a large-eddy simulation of a highly heated laboratory-scale jet. The pressure reconstructions match the near and far

fields with minimal error within the measurement aperture, while reconstructions within the jet plume (where the equivalent wave model no longer applies) underestimate the pressure fluctuations, though generally maintain the correct spectral shape.

Integration of the vector intensity generated by NAH over an enclosing surface predicts the acoustic power level. With knowledge of the mechanical power of the simulated jet, an acoustic efficiency of 1.5% is calculated. Using an axisymmetric assumption is found to be suitable for calculating the acoustic power from this round-nozzled jet. Estimates of the acoustic power using the squared pressure instead of the full pressure and particle velocity calculations overestimate the overall level as little as 1 dB, even in the geometric near-field. However, using the squared pressures in the near field does not accurately localize the source distribution of acoustic power, shifting it aft, leading to an overestimation of power originating from the subsonic portion of the flow.

The simple calculation of the acoustic efficiency of a jet could be easily applied to any simulated jet database which includes the density and velocity at the nozzle exit and the pressure and particle velocities along a FW-H type surface. If axisymmetry is assumed, a single sampled line can be used instead. Using a simple tool, such as the acoustic efficiency of the jet, may be valuable for evaluation of noise reduction technologies to isolate whether the noise reduction is due to a fundamental change in radiation characteristics, or if simply the kinetic energy of the gas exiting the nozzle is being controlled to reduce the radiated noise. Though the acoustical efficiency calculated of this particular jet is larger than that assumed of rockets, the data point provided of this jet is a single one. It would be to the benefit of the rocket and jet noise communities to report their calculations of acoustic efficiency so more robust investigation of this space can be accomplished.

Ray-tracing the vector intensity back to the jet centerline, the axial power per unit length is derived, which shows most of the acoustic power originating from upstream of L_s , similar to experiments of other heated laboratory-scale jets (Greska and Krothapalli, 2008). The strong Mach waves generated by the supersonic portion of the jet are likely the reason, as they dominate in this supersonic region (Leete et al., 2020).

Holography is found to be a robust method of characterizing the acoustic field of a supersonic laboratory-scale jet at high temperature. Energy-based quantities derived from the holographic reconstructions match those calculated from the LES. The axial distribution of acoustic power can be estimated from the NAH reconstruction through ray-tracing the origin of the acoustic intensity field or by evaluating the squared pressures along the nozzle lipline, as has been done in prior work for high-performance military aircraft (Leete et al., 2021; Stout et al., 2015; Wall et al., 2016).

ACKNOWLEDGMENTS

This research was supported in part by the Office of Naval Research through the Jet Noise Reduction Project.

K.M.L. was funded by an appointment to the Student Research Participation Program at the U. S. Air Force Research Laboratory, 711th Human Performance Wing, Human Effectiveness Directorate, Warfighter Interface Division, Battlespace Acoustics Branch administered by the Oak Ridge Institute for Science and Education through an interagency agreement between the U. S. Department of Energy and USAFRL. Distribution A. Approved for public release: distribution unlimited.

Adam, A., Papamoschou, D., and Bogey, C. (2021). "The imprint of vortical structures on the pressure field at the edge of a turbulent high-speed jet," in *AIAA Scitech 2021 Forum 2021*, January 11–15 and 19–21, paper 2021-1184.

Bodony, D. J., and Lele, S. K. (2008). "Current status of jet noise predictions using large-eddy simulation," *AIAA J.* **46**(2), 364–380.

Bres, G. A., and Lele, S. K. (2019). "Modelling of jet noise: A perspective from large-eddy simulations," *Philos. Trans. R Soc. A* **377**(2159), 20190081.

Cho, Y. T., Bolton, J. S., and Hald, J. (2005). "Source visualization by using statistically optimized near-field acoustical holography in cylindrical coordinates," *J. Acoust. Soc. Am.* **118**, 2355–2364.

Du, Y., and Morris, P. (2012). "Numerical investigation of the noise source locations of supersonic jets using the beamformed method," in *50th AIAA Aerospace Sciences Meeting including the New Horizons Forum and Aerospace Exposition*, January 9–12, Nashville, TN.

Eldred, K. M. (1971). "Acoustic Loads Generated by the Propulsion System" (number 8072 in NASA SP), <https://ntrs.nasa.gov/citations/19710023719> (Last viewed March 15, 2022).

Fahy, F. J. (1989). *Sound Intensity* (Elsevier Science Publishing Co., New York).

Faranosov, G. A., Belyaev, I. V., Kopiev, V. F., Zaytsev, M. Y., Aleksentsev, A. A., Bersenev, Y. V., Chursin, V. A., and Viskova, T. A. (2017). "Adaptation of the azimuthal decomposition technique to jet noise measurements in full-scale tests," *AIAA J.* **55**(2), 572–584.

Gee, K. L. (2021). "A tale of two curves and their influence on rocket and supersonic jet noise research," *J. Acoust. Soc. Am.* **149**(4), 2159–2162.

Gee, K. L., Akamine, M., Okamoto, K., Neilsen, T. B., Tsutsumi, S., Teramoto, S., Okunuki, T., and Cook, M. (2017). "Characterization of supersonic laboratory-scale jet noise with vector acoustic intensity," in *23rd AIAA/CEAS Aeroacoustics Conference*, June 5–9, Denver, CO, paper 2017-3519.

Greska, B., and Krothapalli, A. (2008). "On the far-field propagation of high-speed jet noise," in *Proceedings of the ASME 2008 Noise Control and Acoustics Division Conference. ASME 2008 Noise Control and Acoustics Division Conference*, July 28–30, Dearborn, MI, pp. 129–133.

Hald, J. (1989). "STSF—A unique technique for scan-based near-field acoustic holography without restrictions on coherence," *Bruel & Kjaer Technical Review* No. 1.

Harker, B. M., Gee, K. L., Neilsen, T. B., Wall, A. T., and James, M. M. (2019). "Source characterization of full-scale tactical jet noise from phased-array measurements," *J. Acoust. Soc. Am.* **146**(1), 665–680.

Horvay, G., and Nagamatsu, H. (1970). "Supersonic jet noise," in *AIAA Aerospace Sciences Meeting*, January 19–21, West Germany.

Jaeger, S., and Allen, C. (1993). "Two-dimensional sound intensity analysis of jet noise," in *15th Aeroacoustics Conference*, October 25–27, Long Beach, CA.

Jordan, P., Zhang, M., Lehnasch, G., and Cavalieri, A. V. (2017). "Modal and non-modal linear wavepacket dynamics in turbulent jets," in *23rd AIAA/CEAS Aeroacoustics Conference*, June 5–9, Denver, CO.

Laufer, J., Schlinker, R. H., and Kaplan, R. E. (1976). "Experiments on supersonic jet noise," *AIAA J.* **14**, 489–497.

Leete, K. M., Gee, K. L., Liu, J., and Wall, A. T. (2020). "Coherence analysis of the noise from a simulated highly heated laboratory-scale jet," *AIAA J.* **58**(8), 3426–3435.

Leete, K. M., Wall, A. T., Gee, K. L., James, M. M., and Downing, J. M. (2021). "Acoustical holography-based analysis of spatio-spectral lobes in high-performance aircraft jet noise," *AIAA J.* **59**, 4166–4178.

- Liu, J., Corrigan, A. T., Kailasanath, K., and Gutmark, E. J. (2015). "Impact of chevrons on noise source characteristics in imperfectly expanded jet flows," in *21st AIAA/CEAS Aeroacoustics*, June 22–26, Dallas, TX.
- Liu, J., Corrigan, A. T., Kailasanath, K., and Taylor, B. D. (2016). "Impact of the specific heat ratio on the noise generation in a high-temperature supersonic jet," in *54th AIAA Aerospace Sciences Meeting*, January 4–8, San Diego, CA.
- Liu, J., Kailasanath, K., Boris, J., Heeb, N., Munday, D., and Gutmark, E. (2012). "Effect of nozzle-exit flow conditions on the flow and acoustic properties of imperfectly expanded supersonic jets," in *18th AIAA/CEAS Aeroacoustics Conference*, June 4–6, Colorado Springs, CO.
- Liu, J., Kailasanath, K., and Gutmark, E. J. (2017). "Similarity spectra analysis in highly heated supersonic jets using large-eddy simulations," in *55th AIAA Aerospace Sciences Meeting*, January 9–13, Grapevine, TX.
- Löhner, R., Morgan, K., Peraire, J., and Vahdati, M. (1987). "Finite element flux-corrected transport (FEM-FCT) for the Euler and Navier–Stokes equations," *Int. J. Numer. Meth. Fluids* **7**(10), 1093–1109.
- Long, D. (2008). "Evaluation of jet and shock cell noise via acoustic holography," in *46th AIAA Aerospace Sciences Meeting and Exhibit*, January 7–10, Reno, NV.
- Lubert, C. P., Gee, K. L., and Tsutsumi, S. (2022). "Supersonic jet noise from launch vehicles: 50 years since NASA SP-8072," *J. Acoust. Soc. Am.* **151**(2), 752–791.
- Lyrantzis, A. S. (2003). "Surface integral methods in computational aeroacoustics—from the (CFD) near-field to the (acoustic) far-field," *Int. J. Aeroacoust.* **2**(2), 95–128.
- Neilsen, T. B., Vaughn, A. B., Gee, K. L., Swift, S. H., Wall, A. T., Downing, J. M., and James, M. M. (2019). "Three-way spectral decompositions of high-performance military aircraft noise," *AIAA J.* **57**(8), 3467–3479.
- Panda, J., Seasholtz, R. G., and Elam, K. A. (2005). "Investigation of noise sources in high-speed jets via correlation measurements," *J. Fluid Mech.* **537**, 349–385.
- Papamoschou, D., Morata, D., and Shah, P. (2019). "Inverse acoustic methodology for continuous-scan phased arrays," *AIAA J.* **57**(12), 5126–5141.
- Papamoschou, D., Morris, P. J., and McLaughlin, D. K. (2010). "Beamformed flow-acoustic correlations in a supersonic jet," *AIAA J.* **48**(10), 2445–2453.
- Podboy, G. G., Bridges, J. E., and Henderson, B. S. (2010). "Phased array noise source localization measurements of an f404 nozzle plume at both full and model scale," in *Turbo Expo: Power for Land, Sea, and Air*, pp. 179–208.
- Potter, R. (1968). "An investigation to locate the acoustic sources in a high speed jet exhaust stream," NASA CR-101105.
- Schmidt, O. T., and Colonius, T. (2020). "Guide to spectral proper orthogonal decomposition," *AIAA J.* **58**(3), 1023–1033.
- Schmidt, O. T., Towne, A., Rigas, G., Colonius, T., and Brès, G. A. (2018). "Spectral analysis of jet turbulence," *J. Fluid Mech.* **855**, 953–982.
- Shah, P. N., Vold, H., Hensley, D., Envia, E., and Stephens, D. (2015). "A high-resolution continuous-scan acoustic measurement method for turbofan engine applications," *J. Turbomach.* **137**(12), 121002.
- Steiner, R., and Hald, J. (2001). "Near-field acoustical holography without the errors and limitations caused by the use of spatial DFT," *Int. J. Acoust. Vib.* **6**, 83–89.
- Stout, T. A., Gee, K. L., Neilsen, T. B., Wall, A. T., and James, M. M. (2015). "Source characterization of full-scale jet noise using acoustic intensity," *Noise Cont. Eng. J.* **63**(6), 522–536.
- Stout, T. A., Wall, A. T., Gee, K. L., and Neilsen, T. B. (2018). "Obtaining acoustic intensity from multisource statistically optimized near-field acoustical holography," *Proc. Mtgs. Acoust.* **33**(1), 055002.
- Sutherland, L. C. (1993). "Progress and problems in rocket noise prediction for ground facilities," in *15th Aeroacoustics Conference*, October 25–27, Long Beach, CA.
- Taira, K., Brunton, S. L., Dawson, S. T. M., Rowley, C. W., Colonius, T., McKeon, B. J., Schmidt, O. T., Gordeyev, S., Theofilis, V., and Ukeiley, L. S. (2017). "Modal analysis of fluid flows: An overview," *AIAA J.* **55**(12), 4013–4041.
- Tam, C. K. W. (2009). "Mach wave radiation from high-speed jets," *AIAA J.* **47**(10), 2440–2448.
- Tam, C. K. W., Viswanathan, K., Ahuja, K. K., and Panda, J. (2008). "The sources of jet noise: Experimental evidence," *J. Fluid Mech.* **615**, 253–292.
- Unnikrishnan, S., Goparaju, K., and Gaitonde, D. (2018). "Energy-dynamics resulting in turbulent and acoustic phenomena in an underexpanded jet," *Aerospace* **5**(2), 49.
- Varnier, J. (2001). "Experimental study and simulation of rocket engine freejet noise," *AIAA J.* **39**(10), 1851–1859.
- Wall, A. T., Gee, K. L., Neilsen, T. B., McKinley, R. L., and James, M. M. (2016). "Military jet noise source imaging using multisource statistically optimized near-field acoustical holography," *J. Acoust. Soc. Am.* **139**, 1938–1950.
- Walton, J. T., and Burcham, F. W. (1986). "Exhaust-gas pressure and temperature survey of F404-GE-400 turbofan engine," NASA Tech. Memorandum 88273, <https://ntrs.nasa.gov/archive/nasa/casi.ntrs.nasa.gov/19880010923.pdf> (Last viewed March 15, 2022).
- Williams, E. G. (2001). "Regularization methods for near-field acoustical holography," *J. Acoust. Soc. Am.* **110**, 1976–1988.
- Williams, E. G. (2003). "Continuation of acoustic near-fields," *J. Acoust. Soc. Am.* **113**, 1273–1281.